ARTICLE IN PRESS

Nuclear Inst. and Methods in Physics Research, A xxx (xxxx) xxx



Contents lists available at ScienceDirect

Nuclear Inst. and Methods in Physics Research, A

journal homepage: www.elsevier.com/locate/nima



25

27

28

29

30

31

32

33

34

35

36

37

38

39

40

41

42

43

44

45

46

47

48

49

50

Performance of position-sensitive resistive silicon detectors in the Forward Array Using Silicon Technology (FAUST)

L.A. McIntosh ^{a,b,*}, A.B. McIntosh ^a, K. Hagel ^a, M.D. Youngs ^a, L.A. Bakhtiari ^{a,c}, C.B. Lawrence ^{a,b}, P. Cammarata ^{a,b}, A. Jedele ^{a,b}, L.W. May ^{a,b}, A. Zarrella ^{a,b}, S.J. Yennello ^{a,b}

ARTICLE INFO

Keywords: Charge division Resistive silicon Energy defect Multidetector Position-sensitive

ABSTRACT

The silicon telescopes of the Forward Array Using Silicon Technology (FAUST) have been recently upgraded with silicon detectors which use resistive charge-splitting to measure the position of charged particles. This is in addition to the measurement of the total energy that these charged particles deposit in the detector. The upgrade results in increased angular resolution with a much smaller number of signals than silicon strip detectors with similar resolution. A novel method of calibration has been used to demonstrate the efficacy of these position-sensitive detectors, and the detectors have been used in a commissioning experiment.

1. Introduction

2

3

5

6

7

8

9

10

11

12

13

14

15

16

17

18 19

20

21

22

23

24

The Forward Array Using Silicon Technology (FAUST) is a detector array useful for studying nuclear reactions [1]. It provides wide angle coverage for energy measurement and particle ID of charged particles produced in nuclear reactions. Isotopic resolution is achieved using the dE-E technique. The FAUST is useful in studying nuclear dynamics and nuclear thermodynamics in heavy-ion collisions [2–8]. This paper describes the upgrade to FAUST with position-sensitive detectors which afford it excellent position resolution [9]. This improved position sensitivity allows correlation functions to be measured accurately. The details of correlation functions are dependent on the microscopic nucleon–nucleon interaction and thus can in principle provide information about the emergent nuclear equation of state [10]. In addition, correlation functions provide a means of observing extremely short lived resonant states and their interactions with the source that produced them.

2. Forward array using silicon technology (FAUST)

This paper describes the position-sensitive hardware and electronics upgrade of the Forward Array Using Silicon Technology (FAUST) at Texas A&M University. The FAUST consists of 68 silicon-cesium iodide (Δ E-E) telescopes. In order to increase the momentum resolution of light charged particles, FAUST was upgraded as described below using the detectors from Ref. [11] to include position-sensitivity. The telescopes of the FAUST are arranged in five concentric square "rings" with

the center of the front square surface of each detector within a single ring equidistant from the target position as described in [1,9,12], and shown in Fig. 1. The five rings are labeled A, B, C, D, and E, with A at the lowest θ and farthest distance from the target, and E at the highest θ and closest to the target position. Ring A consists of eight detector telescopes, Ring B, twelve, and Rings C–E consist of sixteen telescopes each. These telescopes are arranged in a square within each FAUST ring. The detector telescopes cover forward laboratory angles. Fig. 2 depicts the target position (black point) and the faces of each telescope (colored squares). Each ring is depicted in a different color, and subtends a different range of angles. The black square shows the location of a precision slotted mask used for position calibration, which is discussed in Section 5.2.

Each of the 68 telescopes in FAUST consists of an edge-mounted 2×2 cm-faced ${\sim}300~\mu m$ -thick Si detector backed by a thallium-doped cesium iodide scintillating crystal. The CsI crystals are of differing length depending upon the ring (CsI in Rings A–D are 3 cm, CsI in Ring E are 2.26 cm [13]), optically coupled to a light guide, and read out by a photodiode.

Protective aluminized mylar foils are inserted between the rings to protect the silicon detectors from electrons (delta rays) knocked free of the target when bombarded by the beam. The rings are packed closely so as to provide maximum coverage, which limits the available space for placement of mylar delta ray shields. Each mylar sheet has a square cut for the beam to pass through, so that each charged fragment should pass through only one layer of mylar. The first layer, in front

https://doi.org/10.1016/j.nima.2020.164642

Received 30 January 2020; Received in revised form 10 August 2020; Accepted 7 September 2020 Available online xxxx

0168-9002/© 2020 Elsevier B.V. All rights reserved.

^a Cyclotron Institute, Texas A&M University, College Station, TX 77843, USA

^b Department of Chemistry, Texas A&M University, College Station, TX 77843, USA

^c Department of Physics, Texas A&M University, College Station, TX 77843, USA

^{*} Corresponding author at: Cyclotron Institute, Texas A&M University, College Station, TX 77843, USA. E-mail address: lheilborn@comp.tamu.edu (L.A. McIntosh).

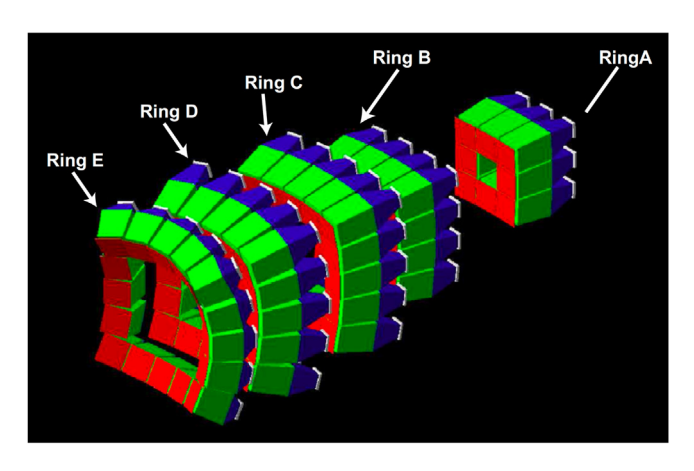


Fig. 1. GEANT4 rendering of the FAUST. Silicon detectors are shown in red, Csl(Tl) crystals shown in green, light guides shown in blue, and photodiodes for light collection shown in white. The faces of the telescopes arranged in five concentric rings in the FAUST point at the target position. (For interpretation of the references to color in this figure legend, the reader is referred to the web version of this article.) *Source:* Figure from Ref. [12].

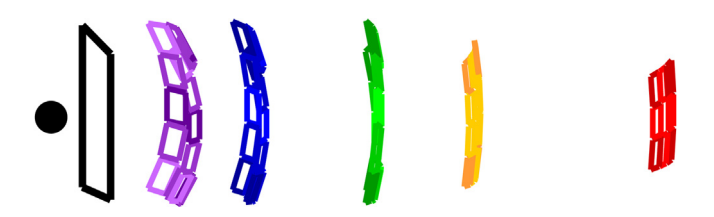


Fig. 2. The orientation of the silicon detectors of FAUST (colored squares) as compared to the target position, shown by the black dot. Beam comes from the left in this figure. The different rings are shown by different colored squares: Ring E (purple), Ring D (blue), Ring C (green), Ring B (orange) and Ring A (red). The front plate (black square) is the only accessible place to put the position-calibrating mask discussed in Section 5.5. (For interpretation of the references to color in this figure legend, the reader is referred to the web version of this article.)

of Ring E, shields both Rings E and D, with a square cut to match the inner edge of Ring D—this layer was 0.833 mg/cm². The second layer, in front of Ring C, shields both Rings B and C, with a square cut to match the inner edge of Ring B and a thickness of 2.535 mg/cm². The last layer, which sits in front of and shields only Ring A, was at the smallest forward angle, so this mylar sheet was the thickest; it was 4.778 mg/cm². The electrons knocked off the target to forward angles have a higher kinetic energy distribution than at less forward angles; more material is required to stop them from reaching the detectors.

The array is used to detect light charged particles in the angular range of 1.6–45.5°. The detectors in the ring closest to the target position (Ring E) cover the largest angular range. The range subtended by the detectors decreases as the rings increase in distance from the target position. Each detector within a given ring sits the same radial distance from the target. Two results of this are that the detectors in the corner of each ring are closer in the beam direction to the target, and that the corner detectors cover a larger angular range than the others.

Altogether, there are thirteen effectively different detector angles, which are depicted with different shades of the color for each ring in Figs. 2 and 3. The telescopes are packed closely together in the FAUST. The geometric $\theta_{\rm lab}$ and $\phi_{\rm lab}$ covered by each detector of the FAUST are shown in Fig. 3; the coverage of each ring is depicted using a different color in the figure (A, red; B, orange; C, green; D, blue; E, purple). The fractional coverage of the array as a function of $\theta_{\rm lab}$ is shown by the black line. This coverage is near 90% for 2–34°, and drops off quickly with increasing $\theta_{\rm lab}$ above that.

The individual telescopes are mounted to an aluminum structure for each of the rings of FAUST. A photograph of the Ring C detectors

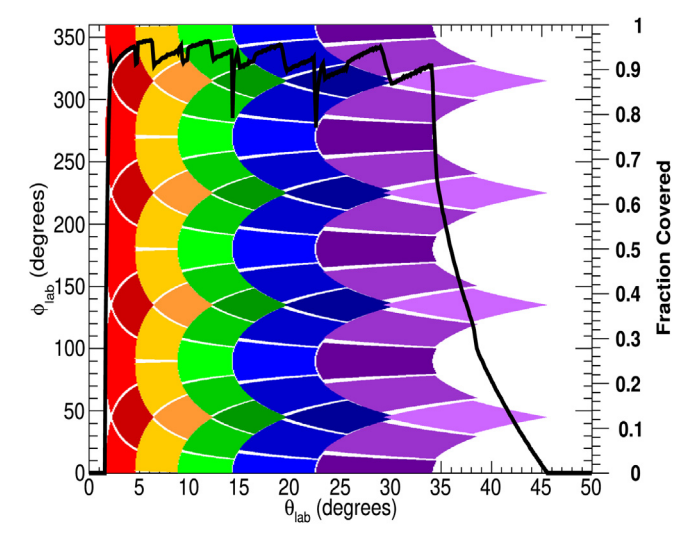


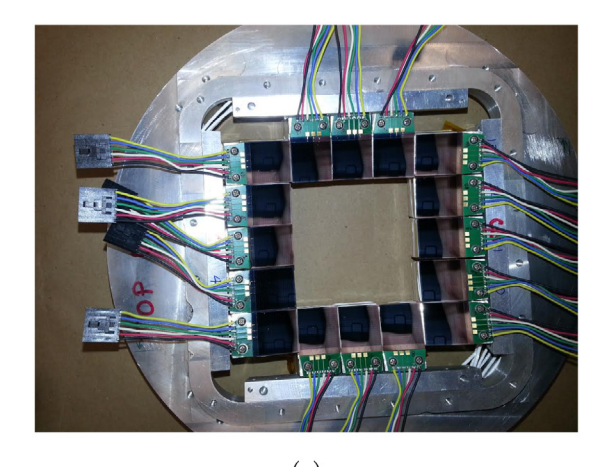
Fig. 3. Angular coverage of the FAUST, shown in ϕ_{lab} (left y-scale) vs. θ_{lab} . The red shaded detectors indicate the two detector positions in Ring A; orange, Ring B; green, Ring C; blue, Ring D; purple, Ring E. The black line indicates the total fraction of azimuthal coverage as a function of the polar angle (right y-scale). (For interpretation of the references to color in this figure legend, the reader is referred to the web version of this article.)

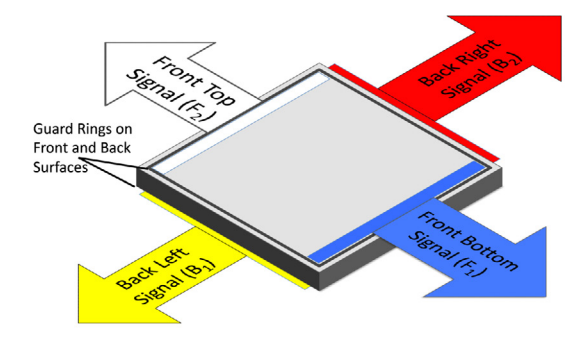
in place on the ring is shown in Fig. 4(a). Following the mounting of the individual detectors, each of the rings are secured in the hollow aluminum cylinder 'cradle', which is in turn mounted in the beamline. A photograph of the fully populated FAUST with detector signal cables is shown in Fig. 4(c) prior to insertion in the beamline.

3. Dual-axis duo-lateral detectors

The FAUST system as originally designed had spatial resolution determined purely by the size of the face of the telescopes and their distance from the target position. An upgrade was carried out to improve the spatial resolution using detectors with a position resolution of 200 µm[11]. Position sensitivity can be achieved with either a resistive electrode or a segmented electrode on the silicon wafer. With the resistive surface, the liberated charge is split in the resistive surface according to Ohm's law, and the relative amplitude of the measured charge pulses is used to determine the position of the incident charged particle. Strip segmentation avoids the charge division, but position resolution is limited by the strip size, the channel count is greatly increased, and charge trapping can occur on the inter-strip dielectric. Though the resistive surface slows the signal rise-times, the impact of this on the energy resolution can be largely mitigated using position-dependent empirical corrections [14]. The most welldocumented disadvantage of resistive technology is the non-linearity of the response (known as a pin-cushion effect), which has been experimentally studied, with a few different approaches to increasing the linearity for the best possible position resolution [11,14-19]. In this paper, we will explain how this defect is overcome for the array. In short, using resistive silicon detectors, we have only four signals per detector to digitize rather than tens of signals per detector, we maintain energy resolution between 1 and 2%, and we obtain 200 μm position sensitivity within a detector.

For the FAUST upgrade, silicon detectors with resistive surfaces on both the front and back faces were chosen [11], known as 'Dual-Axis Duo-Lateral' (DADL) detectors. These detectors were developed in partnership with and fabricated by Micron Semiconductor, Ltd. [20]. The silicon is constructed from n-type $\langle 100 \rangle$ float zone material, with a doping concentration of 4.05E11/cm³. The resistivity is 10 kΩcm. The resistances across the front and the back differ by a factor of two. Therefore, though all signals are used for position, only the front





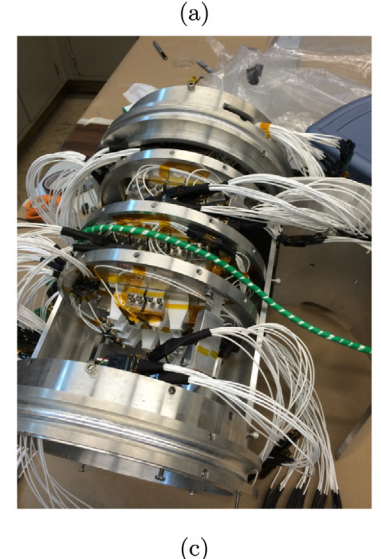




Fig. 4. 4(a). Photograph of Ring C DADL silicon detectors mounted on the ring structure of FAUST, before the ring is added to the FAUST cradle. 4(b). Schematic depiction of DADL detector. The signals from the front of the detector relative to the target position are indicated by white and blue arrows, and represent the holes collected on the front surface. The signals from the back of the detector relative to the target position are indicated by red and yellow arrows, and represent the electrons collected on the back surface. 4(c). Top view photograph of the FAUST fully populated by detector telescopes. This photograph demonstrates the spatial constraints presented by the preexisting FAUST system which dictate where mylar can be placed, as discussed in Sections 2 and 5.5. 4(d). Photograph of one FAUST dE-E telescope. The DADL Si is mounted in the front, the large CsI(Tl) crystal, light guide, and photodiode for readout are behind.

signals are used for energy measurement to the extent possible. The resistive surface layer is about 300 nm thick, about 0.1% of the detector thickness. Such a thickness is typical of silicon detectors, whether they use resistive splitting on the surface or not.

A photograph of a DADL mounted in front of a FAUST CsI is shown in Fig. 4(d). The "front" of the DADL detectors is defined as the surface facing the target position, the "back" is the face oriented towards the CsI(Tl) crystal. The six colored wires there each connect to one of the six electrodes on the surfaces of the DADL detector. The schematic Fig. 4(b) indicates the electrode to which each wire connects. The measured and recorded signals from these four electrodes are referred to as F1 (bottom), F2 (top), B1 (left), and B2 (right).

The 300 µm-thick detector is reverse-biased by applying -40V to the front (both F1 and F2 electrodes) and ground to the back (both B1 and B2 contacts). The front guard ring is biased at -36.4~V with a resistive voltage divider; the back guard ring is held at ground. Because of the resistive surfaces on the detector, the charge splits across the front face according to the vertical position, and across the back face according to the horizontal position. From this charge splitting, the local X and Y are calculated in the following way, where "Q" is the raw charge signal from the detector:

$$X_{\text{Local}} = \frac{Q_{\text{Right}} - Q_{\text{Left}}}{Q_{\text{Right}} + Q_{\text{Left}}}$$
 (1)

nd

$$Y_{\text{Local}} = \frac{Q_{\text{Top}} - Q_{\text{Bottom}}}{Q_{\text{Top}} + Q_{\text{Bottom}}}.$$
 (2)

Conductive stripes of aluminum punctuate the surface of the resistive layer at regular intervals to facilitate the flow of charge to the edges where the charge leaves the detector. These equipotential lines run horizontally across the front surface because the charge splits to local top and bottom on the front. On the back surface of the detector, these lines run vertically because the charge splits to local right and left. The electrodes create a uniform 300 nm dead layer on each face of the detector.

The wires that attach directly to the DADL silicon detectors were secured with kapton tape and buckled to low-capacitance cables to pass through the holes in the cradle. These cables connected to the adapter boards. These PC boards combine the individual signals and guard rings from four DADL detectors into a single 34-pin header cable that attached to a feedthrough in the FAUST chamber wall. Ribbon cables manufactured by 3M (3601/34) made with very low-capacitance (9.9 pF/ft) were used to make these cables. They were surrounded by a hollow grounding braid with a grounding strap inside to allow for connections to reduce noise before the signals reach the preamplifiers outside of the chamber.

Fig. 5. Raw signal processing for the FAUST setup. Electronic signals are indicated by arrows.

The silicon detectors were individually biased to -40V using a Wiener MPod bias supply, detector-by-detector. The photodiodes which read the cesium iodide detectors were also biased using the Wiener MPod, but on a ring-by-ring basis, to 9 V.

4. Electronics

The signal-splitting depending upon position of the particle on the surface DADL detector meant that the amplitude of signals from the silicon detectors were much smaller than had previously been detected in the original FAUST electronics. Also, it was desirable to get as much of the light charged particle distribution as possible. Such particles deposit little energy in Si, making high gain preamplifiers necessary. Preamplifiers of 110 mV/MeV, designed and manufactured by RisCorp Inc. were used to handle the Si signals [21]. Preamplifiers of this design are also discussed in [12], although the FAUST DADL CSA excluded the timing circuitry as unnecessary. Because these preamplifiers are such large gain, keeping the noise to a minimum is very important. A copper wire mesh around the signal cables and preamplifiers during the experiment acted as a Faraday cage and cut down the ambient noise considerably.

The signal processing for silicon and cesium iodide detectors of FAUST is summarized in Fig. 5. The silicon signals were routed through PC boards which distributed front and back signals (which are of opposite polarity) to different Charge Sensitive Amplifiers (CSA), as described above. Cesium iodide signals were amplified by CSAs with a gain of 40 mV/MeV from ZeptoSystems[22]. The Application-Specific Integrated Circuit for HINP (Heavy Ion Nuclear Physics) [23] were used to amplify the signals from the preamplifiers. The peak voltage from each shaper is digitized by analog-to-digital converters mounted on a mezzanine board on the XLM-XXV (JTEC Universal Logic Module). The trigger was generated in the ASIC electronics as an OR of all of the cesium iodide detectors. The digitizer is a 14-bit ADC [23], which digitizes a constant voltage level corresponding to the amplitude of the signal out of the shaping amplifier. The calibrations are described in the next section.

5. Calibrations

5.1. Particle identification

Charged particles deposit energy in the two detectors a of dE-E telescope in a way dependent on their charge and mass. This allows for identification of particles. The isotopic resolution is demonstrated in Fig. 6 where the uncalibrated total energy measured in the silicon detector (F1+F2) is plotted against the uncalibrated energy measurement in the CsI. The characteristic band separation of different particle types allows for visual particle identification. The lowest and left-most band is protons (p), moving to the right are isotopes of hydrogen, helium, lithium and beryllium. In order to identify these particles on a case-by-case basis, the signals detected in the silicon and cesium iodide are processed to linearize the raw signals to get particle identification (PID)

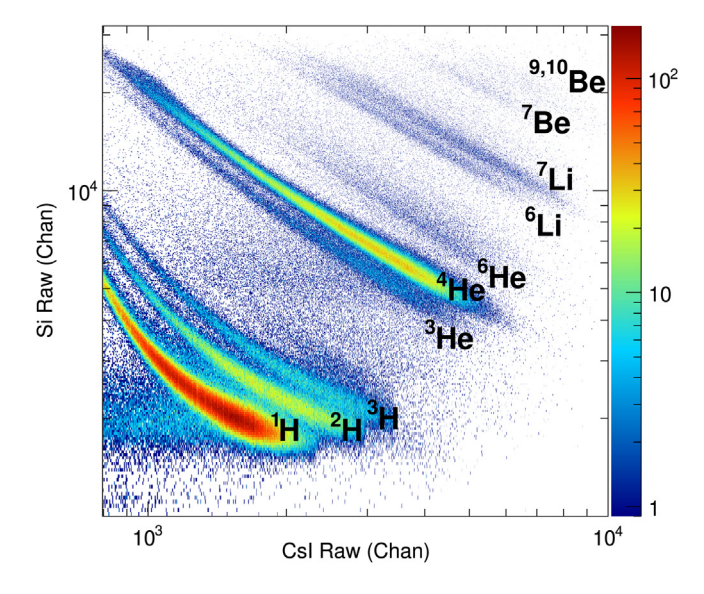


Fig. 6. Raw two-dimensional spectrum of a representative detector (22) showing reaction products from a representative system ($^{40}\text{Ca} + ^{58}\text{Ni}$ at 40 MeV/nucleon), demonstrating the isotopic resolution achieved in this experiment. Note that all three axes are on a logarithmic scale.

values so that simple cuts can be used on PID values to determine particle Z and A.

An equation which is based roughly upon the Bethe–Bloch equation was used to linearize the curves observed in the Δ E-E correlation in the manner used in [24]:

$$PID = b \ln(p_0) - \ln(b\Delta E) - (b - 1) \ln(E + p_1 \Delta E)$$
(3)

where

$$b = p_2 - p_3 \Delta E / p_4, \tag{4}$$

$$\Delta E = m_{Si}C_{Si} + b_{Si} \tag{5}$$

and 54

$$E = m_{CsI}C_{CsI} + b_{CsI} (6)$$

with the p_0 - p_4 parameters varied by hand over a small range of values until linearized. The slopes and intercepts of the CsI and Si (m_{Si} , m_{CsI} , b_{Si} , b_{CsI}) calibrations were also varied by hand. The only significance of the PID values lay in the ability to separate particle types using a single variable, rather than the relationship between the energy deposited in the silicon and cesium iodide and are discussed in [9].

The PID values obtained are plotted versus the energy deposited in the silicon in Fig. 7 for detector 22, a detector in Ring C which is used throughout this paper as a representative. This demonstrates how one-dimensional gates are applied to the PID value distribution to define the particle types.

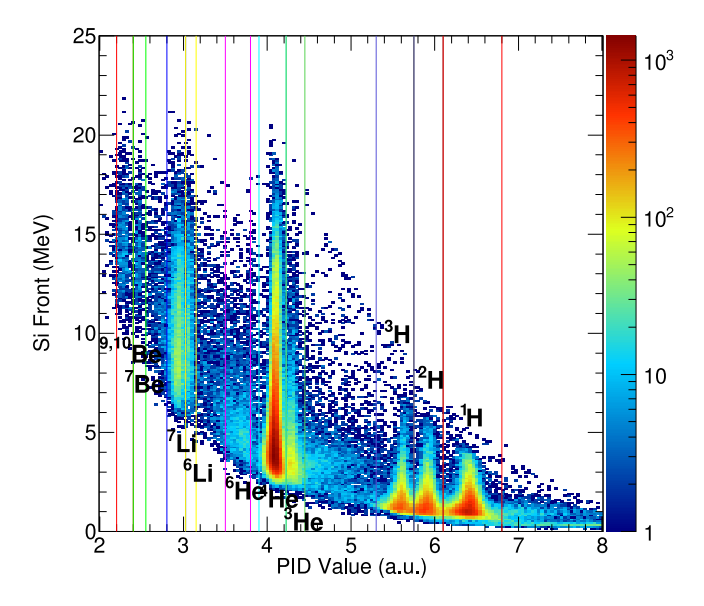


Fig. 7. Two-dimensional spectrum for a representative detector (22) showing reaction products from a representative system (40 Ar+ 58 Fe at 40 MeV/nucleon). Plotted here are the silicon energy vs. the PID value, calculated using Eq. (3). The vertical colored lines indicate how the linearized values are cut in order to identify different particle types.

5.2. Position-dependent energy correction

The position-sensitive capability of the DADL detectors allowed an investigation of and correction for the position-dependent nature of the energy measured in the silicon detector due to the passage of the charge carriers through the resistive surfaces of the Si detectors. By using reaction products from the beam and alpha particles from a source for calibration, we illuminate the entire detector array at once and get information about the relative positions of the detectors. In addition, the continuous distributions provide sufficient statistics over the face of each detector to allow for correction of the energy based on the position in a continuous way.

The signals from the DADL's four electrodes correspond to digitized voltage amplitudes after the ASIC shaping amplifiers, shown in Fig. 5. The threshold for detector 22 is 270 keV for both front signals, and 285 keV for both back signals. In this respect as in many other respects, detector 22 is representative of the detector array. When a $^{228}{\rm Th}$ source is placed in front of the FAUST silicon detectors for calibration, plotting F1 vs. F2 or B1 vs. B2 reveals the six distinct lines of single-energy α particles emitted by the source, shown in Fig. 9a. The bands have a slight curvature to them.

A raw spectrum of F1+F2 is shown in Fig. 9b for 228 Th data. Also shown in Fig. 9b are the peaks for monoenergetic particles in calibration beams provided by the cyclotron (red and green distributions). The FWHM of the highest energy 228 Th peak is 146 channels. This is 1.3%, which can be improved. This sum is approximately proportional to the energy deposited in the detector, but must be corrected for the position defect which arises from the two capacitively coupled resistive surfaces of the detector [25]. In order to correct for the position defect, the sum (F1+F2, raw energy) vs. the difference (F2-F1, raw position) of the raw signals was plotted. This is shown in Fig. 9c with a cut applied to remove small signal amplitudes corresponding to electronic noise. If the apparent energy deposited by the single energy alpha particles were not dependent upon the position at which the alpha particle hit the detector, these lines would be horizontal.

In order to perform the energy calibration of the silicon detectors the position dependence of the signals must be accounted for. A quadratic fit of each of the curved bands corresponding to monoenergetic alpha particles was performed to determine the curvature of the

line (a), the linear component (b), and the y-intercept (c). In this case, when x=0, the alpha particle hit the middle of the detector. The results of these fits can be seen in Fig. 9c. In order to span the broadest energy range possible for the position correction, data from the calibration beams is used in addition to the $^{228}{\rm Th}$ source data. The fit of all of these is shown in Fig. 9c. Alpha particles 1–5 are, in order of descending energy, the alpha particles emitted from the $^{228}{\rm Th}$ source. Alpha 6 is approximately 8.2 MeV, the amount deposited in the Si from the 15 MeV/u α beam. Alpha 7 is the α from the p- α at 10 MeV/u beam, 11.6 MeV.

The non-linear components of this fit are then subtracted from the overall energy to obtain a corrected spectrum and improve the energy resolution. In order to remove the position-dependence of the energy, the "a" and "b" parameters were plotted with respect to "c" so as to characterize the curvature (a) and nonlinearity (b) as linear functions of the energy. The equation for the corrected energy can be written as follows:

$$F_{\text{corr}} = s - b(s)d - a(s)d^2,\tag{7}$$

where F_{corr} is the corrected sum of the front signals, s is the sum of the two signals, d is the difference of the two raw signals, a(s) is determined by the fit of a vs. c and b(s) is determined by the fit of b vs. c [9].

The bands seen in Fig. 9 panel b corresponding to discrete alpha particle energies now no longer exhibit a dependence on position, which improves the effective energy resolution considerably. The resulting position-corrected (but still uncalibrated) spectrum is shown in the bottom of Fig. 9b. Even a merely cursory comparison between Fig. 8b and 9b, which shows the effective resolution of the detector is much improved by this correction. The raw FWHM on the highest energy alpha from the thorium (black) is now 101 channels, or 0.9%. This corresponds to 83 keV for a 9 MeV peak. The raw energy vs. position graph for the back of the detector (closest to the CsI crystal) was fit in an analogous way. Thus the energy determined from the back signals was also corrected.

The cesium iodide detectors were calibrated for Z=1 and Z=2 particles using the energy deposited in the silicon. The non-linearity of the CsI signals was allowed for, correlating the calculated energy from SRIM with the measured signal from the detector using a previously described functional form for protons separately from alpha particles [26–28].

5.3. Missing fourth signal calculation

Particles used in the silicon energy calibration were required to have energy signals above the threshold and below saturation of all four channels of the DADL detector. If one of the four signals on the silicon detector is very small, due to a high-energy charged particle depositing very little energy in the detector, or due to the particle being very close to an edge and therefore leading to highly asymmetric charge splitting across the face of the detector, or both, it is possible to measure three signals above threshold and have a "missing" fourth silicon signal. It is also possible that due to high charge deposition and highly asymmetric charge splitting, one signal is above saturation, and therefore "missing".

For a particle where both of the front signals were measured in the appropriate range, but only one of the back signals was measured, the equivalence of energy measured on the front and the back of the DADL detectors allowed for the reconstitution of the missing back signal. For particles with four signals, the position-corrected sum of the fronts vs. the sum of the back two signals is plotted. A linear fit was applied to these values. This linear fit is used to calculate the total energy deposited in the back of the silicon detector, and then the "missing" back signal is calculated from the back sum and the measured back signal. The analogous process is done to retrieve front signals. This had the desirable effect of increasing the total number of charged particles that could be utilized in subsequent physics analysis.

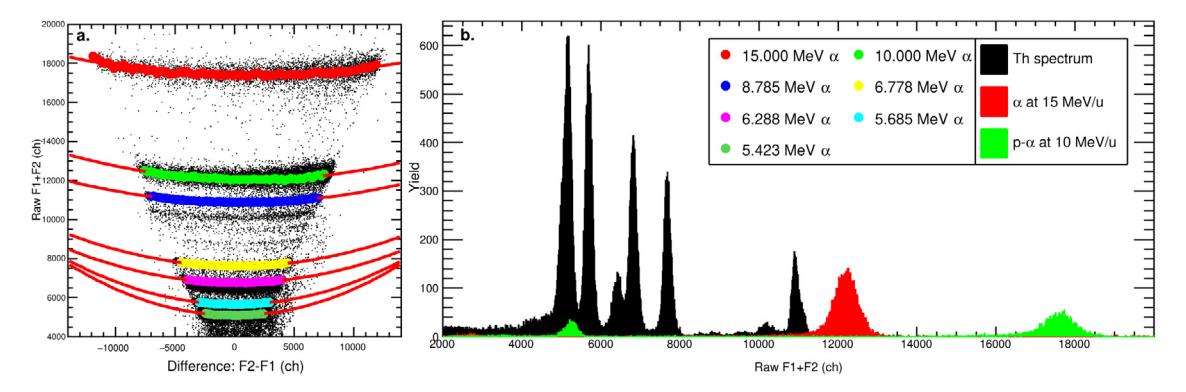


Fig. 8. 8a. Sum vs. difference (raw position) of front signals plotted for 228 Th source and calibration beams of p- α at 10 MeV/nucleon and α at 15 MeV/nucleon on detector 22. 8b. Energy spectrum of the alpha particles emitted by the 228 Th and scattered calibration beams on detector 22.

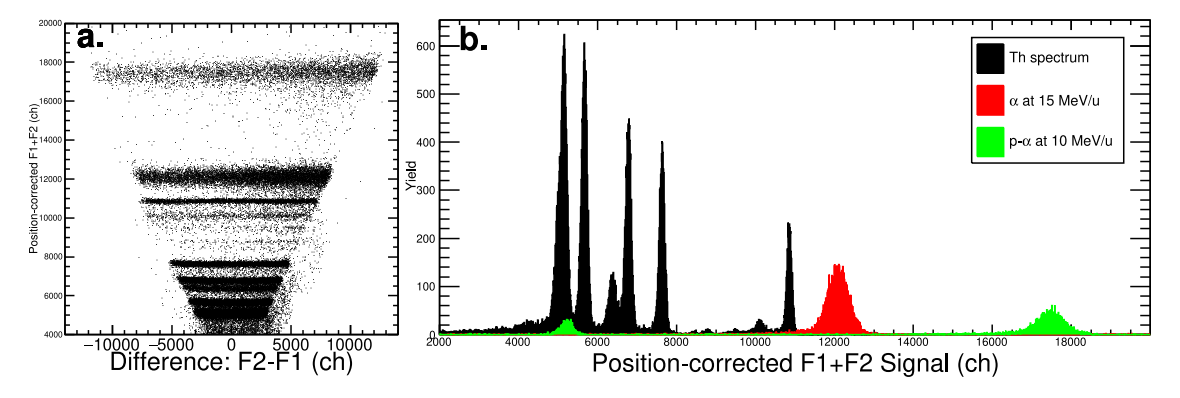


Fig. 9. 9a. Position-corrected sum vs. difference of front signals plotted for 228 Th source and calibration beams of p- α at 10 MeV/nucleon and α at 15 MeV/nucleon on detector 22. 9b. Position-corrected energy spectrum of the alpha particles emitted by the 228 Th on detector 22 and the calibration beams (red and green).

After the finalization of each of the calibrations discussed above, Z and A identified particles that met the energy requirements for their particle type, Fig. 10 shows the normalized energy spectra with the calculated missing fourth silicon signals for protons and alpha particles discussed in Section 5.3. The bulk of the particles retrieved via this process are high energy protons. As shown by the distribution of the red and green histograms on the right of Fig. 10, some alpha particles were also recovered.

1

2

3

4

5

6

7

8

9

10

11

12

13

14

15

16

17

18

19

20

21

22

23

24

25

26

27

28

29

30

31

32

The bulk of the particles that were able to be resurrected via this method were low energy $Z\!=\!1$ particles (threshold effect), although some amount of higher Z particles can also be retrieved. This is crucial for detecting as many protons as possible. About 5% of the total cohort of protons have positions calculated in this method, and 1% for alpha particles.

The range of energy of the particles that were added back into the data set is demonstrated in Fig. 10. These histograms are normalized to demonstrate the difference in the shape of the energy distributions that result from four signal events and those that can be calculated. The protons that were added back from the calculated front and back (red and green) are at a higher average energy than the four signal events (black). They shift the measured energy spectrum higher in energy, as shown in the blue 'All Signals' spectrum. The alpha particle energy spectra (right) do not shift significantly in energy with the addition of the calculated signals, which is evidenced by the fact that the blue and black spectra on the right of Fig. 10 are indistinguishable. This is due to the fact that the number of calculated alpha signals is very small, and not focused on one area of the alpha energy spectrum.

We seek to study how the detector response depends on the particle type, deposited energy, and position within the detector. By measuring light charged particles from nuclear reactions, we simultaneously illuminate the entire detector array with a variety of particle types, each with a broad energy range. The energy and position dependence of the

protons from three-signal events is demonstrated in Fig. 11 for detector 22. The position shown corresponds to the projection of the proton's momentum vector projected onto a plane perpendicular to the beam axis and 3 cm downstream of the target. Each column corresponds to a particular cut on proton kinetic energy, increasing in energy from left to right; 10-20 MeV, 20-30 MeV, 30-40 MeV, and 40-50 MeV. The first row shows the projected Y vs. X position for protons collected using all four (F1, F2, B1, B2) signals from the DADL detector. Particles that deposit a large amount of energy can be measured nearly anywhere in the detector, as even after charge split, all four signals will be above threshold. Particles that deposit slightly less energy can be measured in most of the detector area, but cannot be measured when they are too close to a corner. In this case, one front signal and one back signal would be below threshold, and would not be reconstructable. As the deposited energy decreases, the total area where three of more signals would be above threshold decreases. This is explored in Fig. 11 for protons and 12 for alphas. The effect is significant for protons since their energy loss is small. In the four signal case, as proton energy increases (and deposited energy decrease), the area which provides four signals above threshold (Fig. 11,top row) decreases but retains its aspect ratio. The case of one missing back signal and no missing front signals is shown in Fig. 11 row two, where the missing back is calculated from the three that are measured. Here as proton energy increases, the effective sensitive area becomes short and wide. This is expected since when the deposited energy is very low it must split its energy nearly evenly to pass both front thresholds. A similar argument applies to the missing front signal case in the third row. The events with four detected signals, a calculated back signal, and a calculated front signal are added together and shown in the fourth row. The bottom two rows of Fig. 11 show the one-dimensional projections of the X and Y positions for the first three rows. The differences between the X and Y distributions may be due to the difference in resistance across the front

33

34

35

36

37

38

39

40

41

42

43

44

45

46

47

48

49

50

51

52

53

54

55

57

58

59

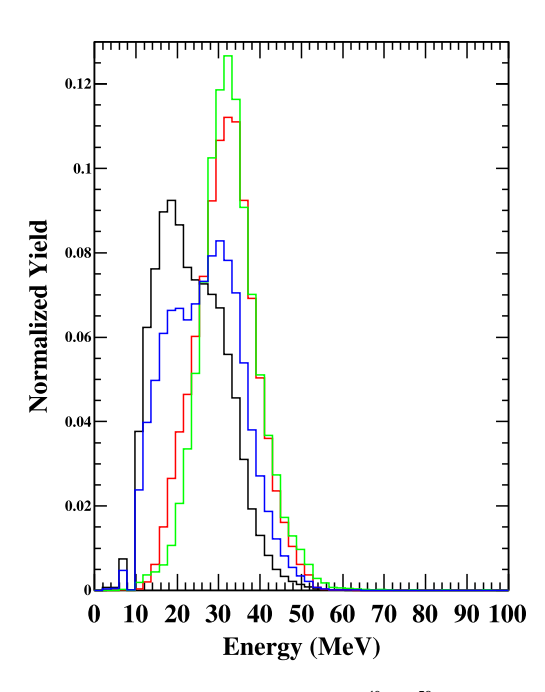
61

63

64



Alpha Particles



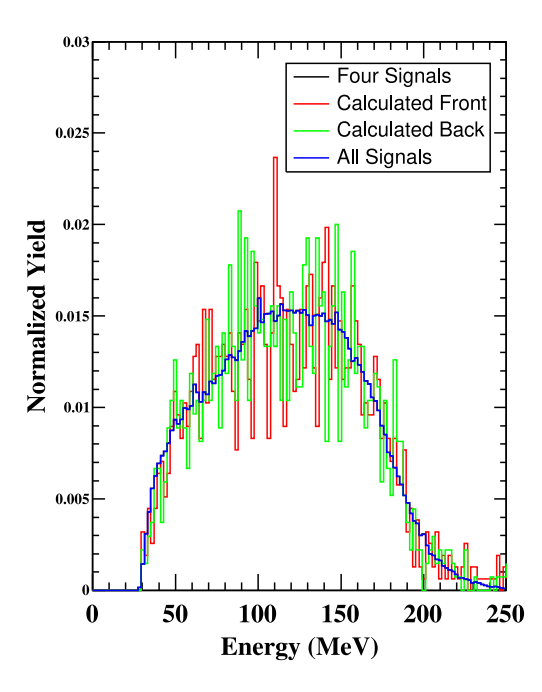


Fig. 10. Representative detector 22 for representative system (40 Ca+ 58 Ni at 40 MeV/nucleon). Energy spectra for protons (left) and alpha particles (right) that had five (4 Si + CsI) acceptable signals (black) and were added in as a calculated missing front (red) or back (green) signal. All spectra are drawn normalized, for perspective the sum of the black, red, and green spectra is also drawn in blue, marked "All Signals". For the protons (Left Panel) 63% of the particles have Four Signals detected, 29% are added using the Calculated Front, and 8% are added back using the Calculated Back. For the alpha particles (Right Panel), more than 99% of the particles have Four Signals detected, less than 0.5% are added using the Calculated Front, and less than 0.5% are added using the Calculated Front and Back histograms are due to low statistics. (For interpretation of the references to color in this figure legend, the reader is referred to the web version of this article.)

and the back of the detector as well as slightly different thresholds for the front and back channels. When the particle information is possible to reconstruct from three signals, the energy and position are measured well. When it is not possible to reconstruct because more than one signal is below threshold, the particle is discarded. This results in a large area of the detector being sensitive to low energy protons, and a smaller portion of the detector being sensitive to high energy protons but with no less accuracy.

2

3

4

5

6

7

8

9

10

11

12

13

14

15

16

17

18

19

20

21

22

23

24

25

26

27

28

29

30

31

32

33

34

35

The energy-dependence of the alpha particles whose existence can be extracted from calculating missed front or back signals is demonstrated in Fig. 12. Each column corresponds to a particular cut on alpha particle kinetic energy, increasing in energy from left to right; 50-100 MeV, 100-125 MeV, 125-150 MeV, and 150-175 MeV. The first row shows the projected Y vs. X position for alpha particles collected using all four (F1, F2, B1, B2) signals from the DADL detector 22. Moving from the lowest energy alpha particles to the highest energy alpha particles, the effective size of the face of the detector does not decrease as dramatically as it did for protons in Fig. 11. This is because the alpha particles deposit more energy in the detector than protons, which makes it more difficult for any of the signals to be lost due to being below the energy threshold. There is a very slight pincushion shape observed in the position map which is due to the capacitive coupling of the resistive surfaces of the detector [25]. The alpha particles retrieved when a back signal is calculated are shown in the second row. These alpha particles are distributed equally across the face of the detector, they do not demonstrate the same positiondependence that the protons do. The alpha particles retrieved when a front signal is calculated are shown in the third row. The events with four detected signals, a calculated back signal, and a calculated front signal are added together and shown in the fourth row. The bottom two rows of Fig. 12 shows the one-dimensional projections of the X and Y positions for the first three rows. The Y positions are not symmetric about the center due to the fact that positions in lower projected Y space for this detector are closer to the beam axis than the higher Y positions, and are therefore favored.

5.4. Calibrations of silicon energy

Following the position correction, the centroid of each peak from the thorium spectrum was calculated, and a linear calibration from corrected channel to energy was obtained. Aluminized mylar was in front of the silicon detectors to act as a delta ray shield, as discussed in Section 2. The effective thickness of the mylar varies across the face of the detector with a 1/cos dependence. While one could randomly sample (e.g. Monte Carlo) the energy loss across the entire face of the detector and take the average energy loss, there is a 1% error at worst using the effective mylar thickness only at the center position of each detector. Due to the fact that these sheets are very thin, this mylar essentially has only a small effect on nuclei coming from the target during the experiment; this energy loss is smaller than the resolution of the detector telescope. However, when a ²²⁸Th source is set at the target position for the purpose of calibrating the silicon detectors, the effective thickness of mylar through which the α particles are degraded is significant, and depends on the angle (θ) of each detector. For the calibration beams, the energy loss in the target was about 2% in the target, and about 1% in the mylar delta ray shields. These energy losses have been accounted for in the calibration, the details of which can be found in [9]. This mylar, of varying thickness in front of different rings as discussed in Section 2, was taken into account in determining the incident energy of the alpha particles using the SRIM (The Stopping and Range of Ions in Matter) range tables [26,27]. The energy resolution for the highest energy alpha (8.785 MeV) was below 2% for all detectors, though many were significantly better; for example, detector 22 above had around 0.9% resolution around 9 MeV.

The silicon energy extracted from the front signals and the back signals of the DADL were required to be within 300 keV or 5% of one another (whichever is greater) in order for the particle to be kept. About 5% of the data does not pass this energy requirement.

The calibration beams, used for checking the energy calibrations of both Si and CsI(Tl) detectors and checking the position information

36

37

40

41

42

43

44

45

47

48

49

50

51

52

53

54

55

56

57

58

59

60

61

62

63

64

65

66

67

68

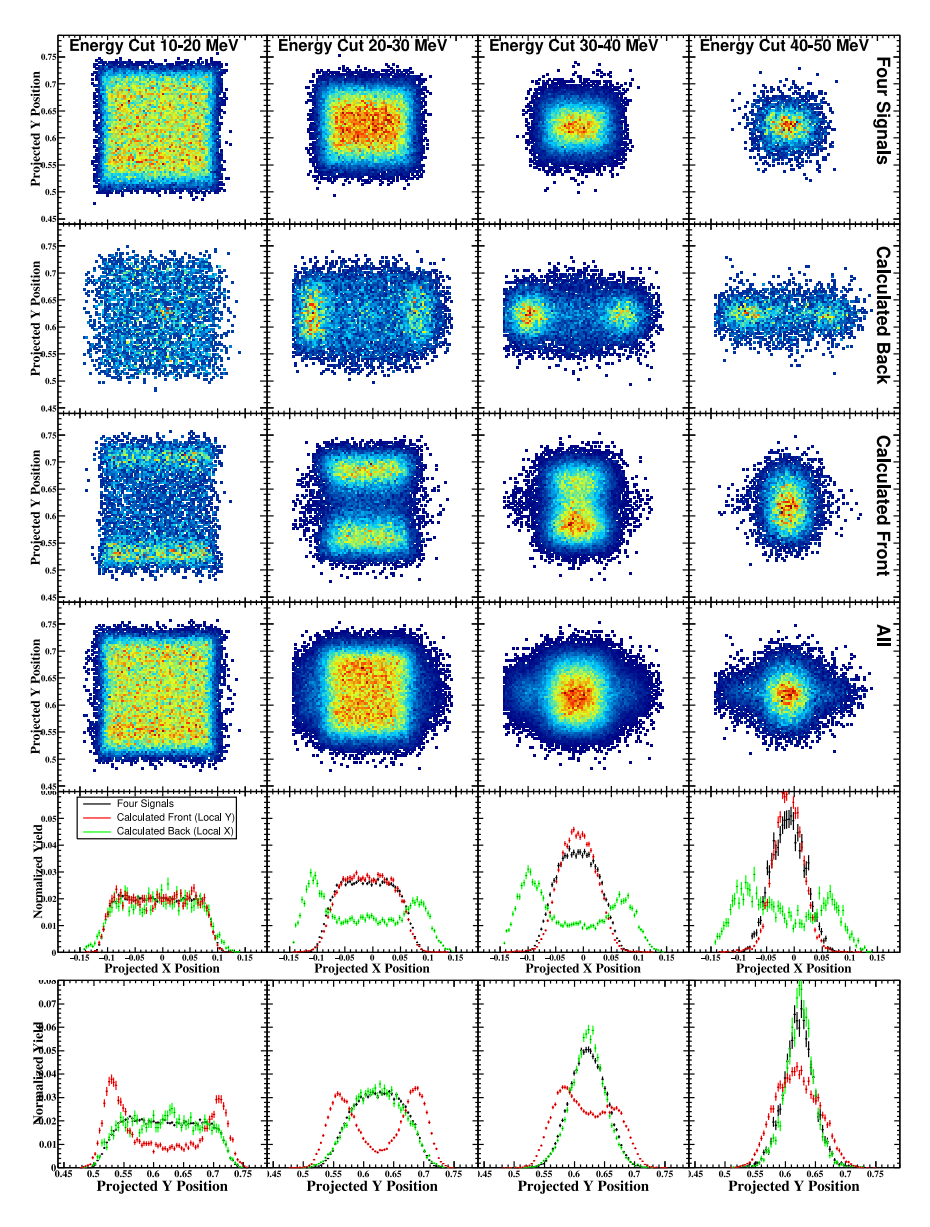


Fig. 11. Protons detected in detector 22. Top line: Four signal events. Second: Calculated Backs. Third: Calculated Fronts. Fourth: Total positions. Fifth: One-dimensional projected x-positions. Sixth: One-dimensional projected y-positions. The columns correspond to energy cuts, increasing in energy from left to right (10–20 MeV, 20–30 MeV, 30–40 MeV, 40–50 MeV total energy for the protons).

from the Si detectors, were 15 MeV/nucleon α and 10 MeV/nucleon p- α , both elastically scattered off of the thick ¹⁹⁷Au target. For some of the measurement period, the Au target was covered by a thick Al collimator with a hole of 1 mm in diameter, to approximate a point source. This method was used for acquisition of both beam and source data with the mask (described in Section 5.5). All of the aforementioned beams were accelerated using the K500 cyclotron at the Cyclotron Institute at Texas A&M University.

5.5. Position determination

Once the DADL detectors are mounted in the FAUST cradle and aligned in the beam, it was important to know that the position-sensitivity of the signals was working properly and all of the local-to-global transposing of the position signals was correct. In order to do this and allow finer calibration of the detector-to-detector relative position in the future, to maximize the benefit of the improved angular resolution of the silicon detectors, some method had to be devised. The mylar foils present in front of the silicon detectors added a degree of difficulty to this endeavor, as the silicon detectors are not optically

visible from the target position once FAUST is assembled and in place in the beamline. A method needed to be developed to project specific shapes via source alpha particles or elastically scattered calibration beams from the target position uniquely across all detectors of the FAUST while in place in the beamline. The only region that is accessible at this point for insertion of the mask is the target location and very front of the FAUST system.

The complexity of this problem is compounded by the unique angling of the detectors at the different positions in FAUST. The Ring A detectors (red squares in Fig. 2 are 40 cm away from the target position, so the pattern needed to be very small on the frontplate of FAUST to be visible on a 2×2 cm detector 37 cm away. The photograph in Fig. 4(c) shows the FAUST cradle with all detectors and cables in place, demonstrating the space constraints solved by the mask design shown in Fig. 13. The engineering challenge is demonstrated in Fig. 2, which shows the orientation of the silicon detectors (colored squares) relative to the mask position. The front plate (black square) is the only accessible place to put a position-calibrating mask. The Ring E detectors (purple squares) are angled sharply, to face the target position outside

Energy Cut 100-125 MeV

Energy Cut 125-150 MeV Energy Cut 150-175 MeV

n<mark>erav Cut 50-100 M</mark>eV

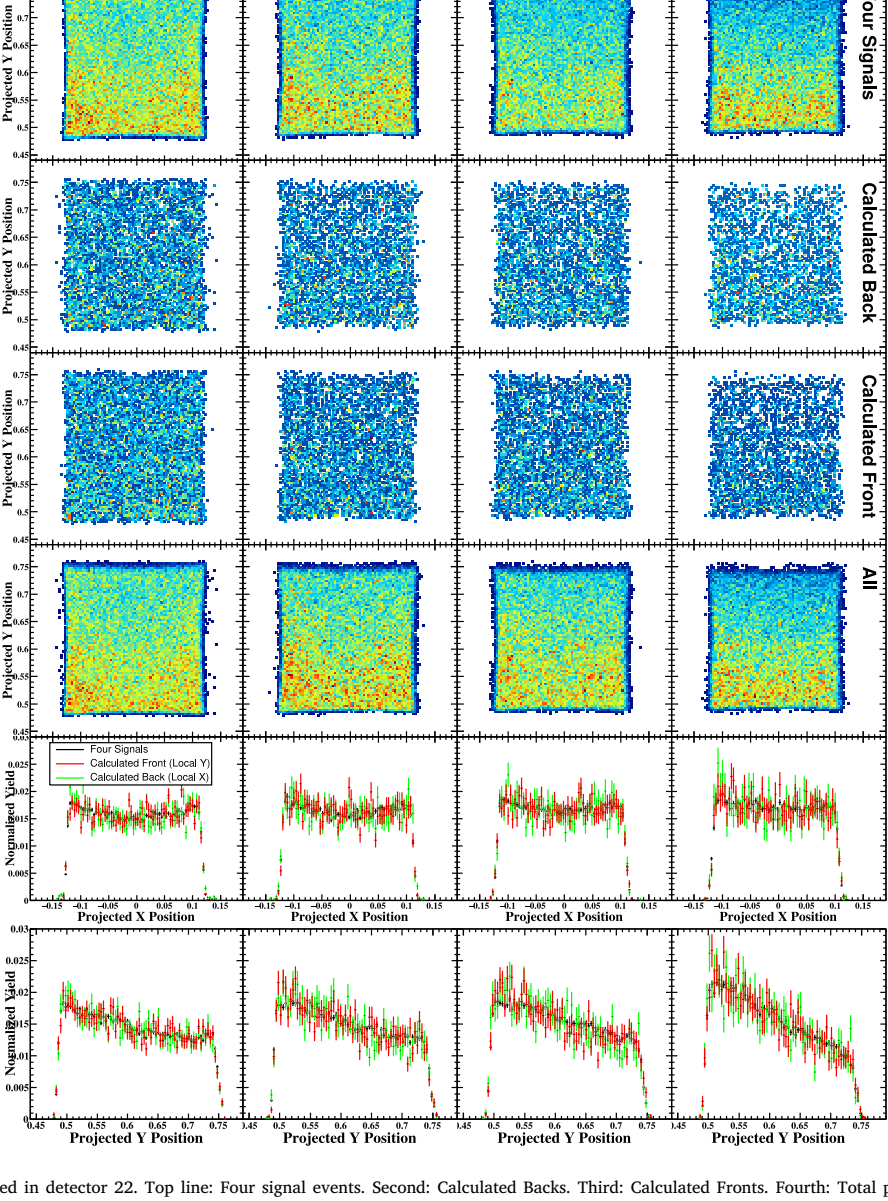


Fig. 12. Alpha particles measured in detector 22. Top line: Four signal events. Second: Calculated Backs. Third: Calculated Fronts. Fourth: Total positions. Fifth: One-dimensional projected x-positions. Sixth: One-dimensional projected y-positions. The columns correspond to energy cuts, increasing in energy from left to right (50–100 MeV, 100–125 MeV, 125–150 MeV, 150–175 MeV total alpha particle energy).

of the frontplate. The mask needed to be able to project a recognizable, orienting pattern on all of the detectors, from Ring A to Ring E.

The front plate of FAUST is designed to shield the detectors of FAUST from charged particles originating upstream of the target position. The mask needed to be set back into the front plate. FAUST was modified to allow the insertion of the striped mask immediately downstream of the target position to block particles in a recognizable pattern.

A slotted tungsten mask was designed to sit 3 cm downstream of the target position between the target and the FAUST array. The slots were angled to allow the passage of particles only in narrow and well defined angular ranges. The tungsten needed to be thick enough to stop 60 MeV alpha particles and 10 MeV protons. The design is shown in Fig. 13. The left figure shows where the angled slits hit the front (solid) and back (dashed) of the mask, where all of the slits are slanted at the appropriate angle to allow passage of particles into the FAUST detectors. This is because the detectors are at many different angles from the target position, as demonstrated in Fig. 2. The middle rectangle shows a side view of the mask (note dashed center line) with

the target position to the left, FAUST silicon detectors to the right. The far right of the figure shows a zoomed in cutaway view from the side, where the middle stripe is perpendicular to the plane of the mask, while the lowest stripe has the maximum angle, to reach the detectors with the largest θ in Ring E.

2.2

A tungsten mask meeting these specifications was manufactured by wire EDM by Reliable EDM in Houston, TX. The mask allowed each of the detectors to "see" the collimated source or scattered α beam. The mask was used in-beam and with a collimated thorium source. The resistive charge splitting described in Section 3 allows calculation of a local position on the face of the silicon detector (front or back) using the ratio of the difference to the sum of the two signals (F1, F2 or B1, B2, Eqs. (1) and (2)). The silicon detectors are 2×2 cm squares, so the local position of the particles hitting the surface of the detector should cover the range from -1 to 1 cm in X and Y in detector coordinate frame. In fact, less than that full range is populated. This is due, at least in part, to external resistors (261 Ohm) placed in series with the detector electrodes. Therefore, a scaling of both X and Y positions to cover the

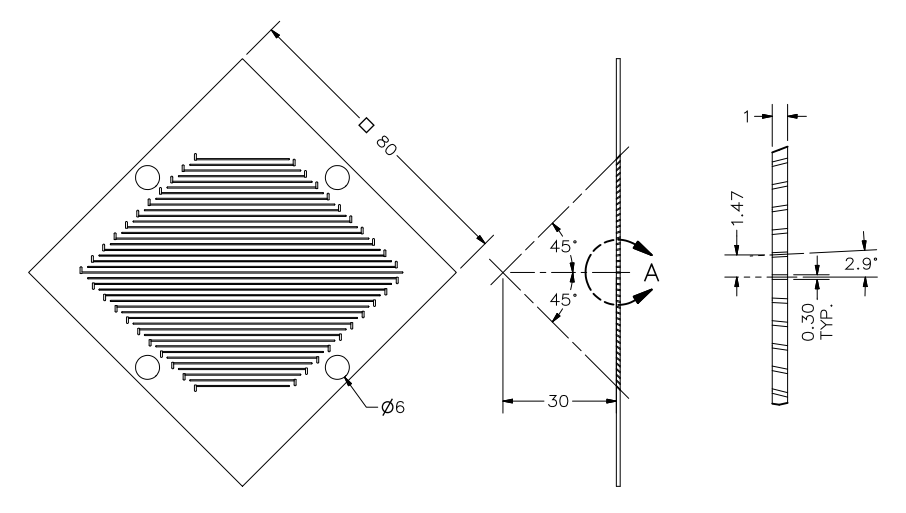


Fig. 13. CAD drawing of the tungsten mask. On the left is the mask shown from the target position, rotated 45° clockwise. The two panels to the right shown cutaway views of the mask (total and zoomed in) demonstrating the different angles of the slits, calculated to hit all of the DADL detectors.

allowable detector coordinate frame was incorporated to compensate for this

These local positions were then transposed to their array coordinate frame within the FAUST using the corners of the detector within the array. A projection of these array coordinate frame onto a plane 3 cm from the target (in the front plate of FAUST) position results in the splatter plots shown. For several detectors, a transposition of two signals was easily caught and corrected by looking at the apparent orientation of the stripes. The resulting alignment of the stripes is shown in Fig. 14 for the elastically scattered p- α calibration beam. The detectors which are closest to the beam axis (Ring A) show stripes with the highest statistics with the scattered beam. These detectors cover the smaller angular range, so fewer stripes are projected on the detectors of the inner rings. Many more stripes are visible on the Ring E detectors, which subtend a much larger angle.

Rings C–E are shown with greater advantage when a source is masked from the detectors. The data obtained by shining a collimated ²²⁸Th source through the mask onto the detectors is shown in Fig. 15. Because the alpha particles from the source are emitted isotropically, the stripes on Ring E are more filled out in this spectrum. All of the telescopes in the FAUST are the same size, so the projected size is just dependent upon the distance between the target and the detectors.

The variability in relative position of the silicon surface once the detector is fully mounted in the beamline, with all of the points of connection, is less than 1 mm, which translates to an angular uncertainty of less than one degree for Ring E, and better for rings successively farther away. The treatment of the raw position signals described in Section 3 gives a local X and Y position on the detector. Due to offsets in the electronics, the area these local positions cover can be somewhat less than the 2×2 cm covered by the DADL detectors. This is accounted for by a stretching parameter in the calibration database, which increases the local position to cover the appropriate amount of area, while taking into account the fact that the guard ring means that the active area of the detectors does not go to the physical edge of the detector. When the positions of stripes of alpha particles on the detector are viewed in detector coordinate frame, large differences in gain between the two front or two back signals would be apparent in a compressed version of the anticipated striped pattern on the detector. Regularly sized stripes across the detector faces, properly aligned, indicate that the positions are consistent with a good position calibration. This is verified even more accurately by examining correlation functions for well-known light-charged particle resonances [9].

6. Summary

FAUST has been upgraded with dual-axis dual-lateral silicon detectors which provide good position resolution (<200 µm, according to

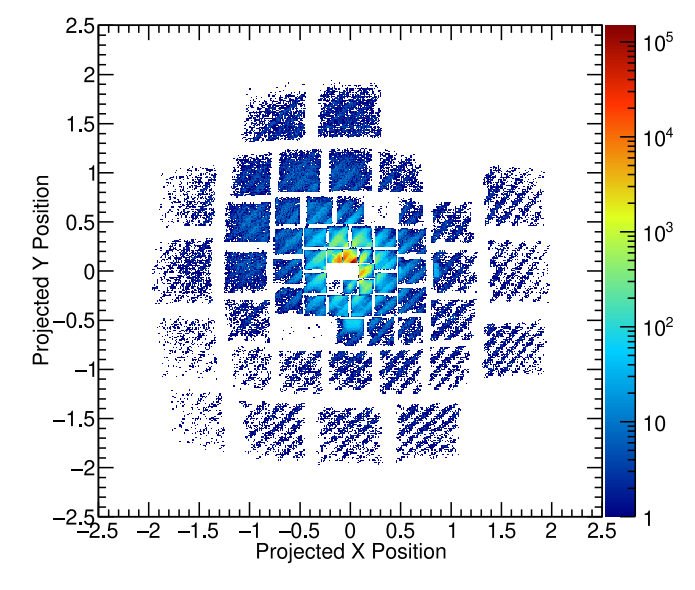


Fig. 14. Projection of the elastically scattered calibration beam alpha particles from the molecular p- α at 10 MeV/nucleon hitting the detectors of the FAUST through the tungsten mask.

Ref. [11]). Not only does this increase the silicon channel count by a factor of four, but the resistive charge division greatly decreases the amplitude of the analog signals that must be digitized and recorded. To address the increase in the number of signals, high-density ASIC shaping amplifiers were used.

By virtue of the nature of the two orthogonal resistive surfaces on the DADL, there is a modest dependence of the measured energy on the position. This dependence is straightforwardly corrected using a series of mono-energetic particles incident over the face of the detector.

A precision slotted mask was designed and fabricated to allow particles to arrive only at certain regions of the DADL detectors. This allows for the array coordinate frame calibration of the detector telescope array to be verified.

To recover the smallest signals, which do not trigger their discriminator, a procedure using three measured signals provides a good reconstruction of the fourth. This is important for measuring the high-energy component of the proton kinetic energy spectrum, and for maximizing the effective useful area of each of the detectors in the array.

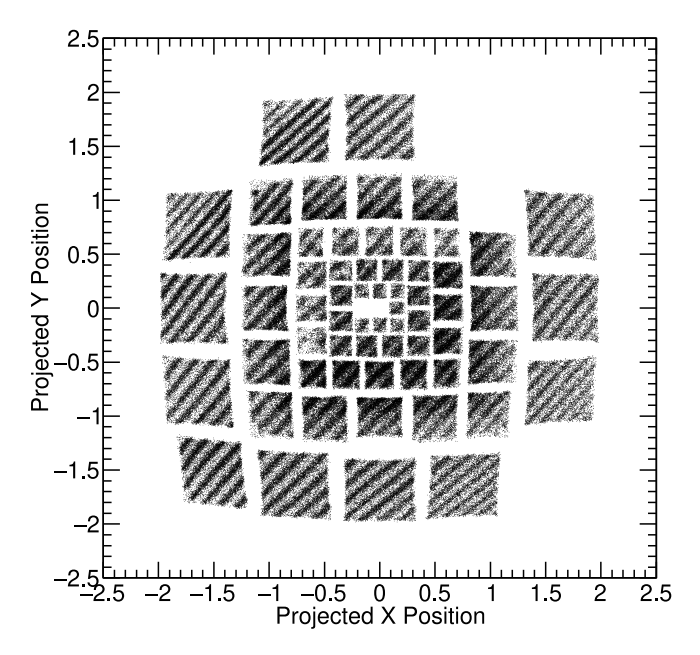


Fig. 15. Projection of the 228 Th source alpha particles hitting the detectors of the FAUST through the tungsten mask.

This upgrade provides high angular resolution, and maintains good energy resolution and particle identification capabilities to the FAUST. This upgrade opens up new measurement possibilities. Correlation functions, in particular, which were only possible very crudely prior to this, can now be done with precision, as shown in Ref. [9]. Analysis of proton–proton correlation functions in reactions of Ca+Ni, Ar+Fe, Ar+Zn @ 30 and 40 MeV/nucleon is underway. Additionally, light charged particles produced in Kr+C @ 15, 25, and 35 MeV/nucleon have been measured and analysis is currently underway.

CRediT authorship contribution statement

L.A. McIntosh: Formal analysis, Investigation, Project administration, Software, Writing - original draft, Writing - review & editing. A.B. McIntosh: Investigation, Methodology, Visualization, Writing - review & editing. K. Hagel: Software. M.D. Youngs: Investigation, Methodology. L.A. Bakhtiari: Investigation. C.B. Lawrence: Investigation. P. Cammarata: Investigation. A. Jedele: Investigation. L.W. May: Investigation. A. Zarrella: Investigation. S.J. Yennello: Conceptualization, Funding acquisition, Resources, Supervision, Writing - review & editing.

Declaration of competing interest

The authors declare that they have no known competing financial interests or personal relationships that could have appeared to influence the work reported in this paper.

Acknowledgments

This work was supported by the U.S. Department of Energy DOE, USA [Grant DE-FG02-93ER40773], the Robert A. Welch Foundation, USA [Grant A-1266], and Department of Energy, National Nuclear Security Administration, under Award Number DE-NA0003841, the Center for Excellence in Nuclear Training And University-based Research (CENTAUR). We would like to thank the excellent staff at the Texas A&M University Cyclotron Institute for providing the experimental beams and technical support. The ASICs were funded by the U.S. Department of Energy grant DE-SC0004972.

References

- [1] F. Gimeno-Nogues, D.J. Rowland, E. Ramakrishnan, S. Ferro, S. Vasal, R. Gutierrez, R. Olsen, Y.-W. Lui, R. Laforest, H. Johnston, S.J. Yennello, FAUST: A new forward array detector, Nucl. Instrum. Methods A 399 (1997) 94–100, http://dx.doi.org/10.1016/S0168-9002(97)00923-6.
- [2] R. Laforest, E. Ramakrishnan, D.J. Rowland, A. Ruangma, E.M. Winchester, E. Martin, S.J. Yennello, Dependence of projectile fragmentation on target N/Z, Phys. Rev. C 59 (1998) 2567–2573, http://dx.doi.org/10.1103/PhysRevC.59. 2567
- [3] M. Veselsky, R.W. Ibbotson, R. Laforest, E. Ramakrishnan, D.J. Rowland, A. Ruangma, E.M. Winchester, E. Martin, S.J. Yennello, Effect of nucleon exchange on projectile multifragmentation in the reactions of ²⁸Si+¹¹²Sn and ¹²⁴Sn at 30 and 50 MeV/nucleon, Phys. Rev. C 62 (2000) 064613–1–10, http://dx.doi.org/10.1103/PhysRevC.62.064613.
- [4] M. Veselsky, R.W. Ibbotson, R. Laforest, E. Ramakrishnan, D.J. Rowland, A. Ruangma, E.M. Winchester, E. Martin, S.J. Yennello, Isospin dependence of isobaric ratio Y(³H)/Y(³He) and its relation to temperature, Phys. Lett. B 497 (2001) 1–7, http://dx.doi.org/10.1016/S0370-2693(00)01318-6.
- [5] S.J. Yennello, M. Veselsky, R. Laforest, D.J. Rowland, E. Ramakrishnan, A. Ruangma, E.M. Winchester, E. Martin, Distribution of isospin during fragmentation of excited quasiprojectiles from the reactions of ²⁸Si+^{112,124}Sn at 30 and 50 MeV/nucleon, Nuclear Phys. A 681 (2001) 317c-322c, http://dx.doi.org/10.1016/S0375-9474(00)00534-0.
- [6] D.J. Rowland, R. Laforest, E. Ramakrishnan, M. Veselsky, E.M. Winchester, A. Ruangma, E. Martin, S.J. Yennello, Formation of excited systems with a wide range in N/Z, Phys. Rev. C 67 (2003) 064602, http://dx.doi.org/10.1103/ PhysRevC.67.064602.
- [7] M. Veselsky, G.A. Souliotis, S.J. Yennello, Isoscaling in peripheral nuclear collisions around the Fermi energy and a signal of chemical separation from its excitation energy dependence, Phys. Rev. C 69 (2004) 031602, http://dx.doi. org/10.1103/PhysRevC.69.031602.
- [8] S.N. Soisson, A. Botvina, G.A. Souliotis, B.C. Stein, L. Heilborn, A.L. Keksis, Z. Kohley, L.W. May, D.V. Shetty, S. Wuenschel, S.J. Yennello, Multifragmentation of reconstructed quasiprojectiles in the mass region A ~30, J. Phys. G: Nucl. Part. Phys. 39 (2012) 115104, http://dx.doi.org/10.1088/0954-3899/39/11/115104.
- [9] L.A. Heilborn, Proton-proton correlation functions measured using positionsensitive FAUST (Ph.D. thesis), Texas A& M University, 2018.
- [10] L. Chen, V. Greco, C. Ko, B. Li, Effects of symmetry energy on two-nucleon correlation functions in heavy-ion collisions induced by neutron-rich nuclei, Phys. Rev. Lett. 90 (162701) (2003) http://dx.doi.org/10.1103/PhysRevLett.90.
- [11] S. Soisson, et al., A dual-axis dual-lateral position-sensitive detector for charged particle detection, Nucl. Instrum. Methods A 613 (2) (2010) 240–244, http: //dx.doi.org/10.1016/j.nima.2009.11.053.
- [12] P. Cammarata, M. Chapman, A.B. McIntosh, G.A. Souliotis, L. Bakhtiari, S. Behling, G. Bonasera, L.A. Heilborn, J. Mabiala, L.W. May, A. Raphelt, M.D. Youngs, A. Zarrella, S.J. Yennello, Studying heavy-ion collisions with coverage near zero degrees using FAUST-QTS, Nucl. Instrum. Methods A 792 (2015) 61–66, http://dx.doi.org/10.1016/j.nima.2015.04.054.
- [13] A.L. Keksis, N/Z equilibration in deep inelastic collisions and the fragmentation of the resulting quasiprojectiles (Ph.D. thesis), Texas A&M University, 2007.
- [14] K. Ieki, M. Ogiwara, Y. Ando, N. Iwasa, H. Murakami, T. Motobayashi, A new method of position determination for a two-dimensional position-sensitive detector, Nucl. Instrum. Methods A 297 (1990) 312–314, http://dx.doi.org/10. 1016/0168-003(00)01390. T.
- [15] T. Doke, J. Kikuchi, H. Yamaguchi, S. Yamaguchi, K. Yamamura, A new two-dimensional position sensitive detector with a good linear response, Nucl. Instrum. Methods A 261 (1987) 605–609, http://dx.doi.org/10.1016/0168-9002(87)90377-9.
- [16] W. Morawek, U. Gollerthan, W. Schwab, K.-H. Schmidt, Correlation technique with a new two-dimensional position sensitive detector, Nucl. Instrum. Methods A 258 (1987) 82–86, http://dx.doi.org/10.1016/0168-9002(87)90082-9.
- [17] N. Colonna, E. Lisi, An analytical method for position reconstruction in twodimensional position-sensitive silicon detectors, Nucl. Instrum. Methods A 334 (1993) 551–556, http://dx.doi.org/10.1016/0168-9002(93)90820-8.
- [18] E. Lisi, N. Colonna, Position reconstruction in two-dimensional position-sensitive silicon detectors: a new analytical method, Nucl. Instrum. Methods A 348 (1994) 703–706, http://dx.doi.org/10.1016/0168-9002(94)90829-X.
- [19] M.-Z. Huang, R.-J. Shen, Y.-X. Wang, X.-M. Dou, Linearity analysis for position sensitive detectors using finite element method, Nucl. Instrum. Methods A 556 (2006) 445–450, http://dx.doi.org/10.1016/j.nima.2005.10.028.
- [20] Micron Semiconductor Ltd, 1 Royal Buildings, Lancing, Business Park, West Sussex, BN15 8SJ, UK, www.micronsemiconductor.co.uk.
- [21] R. Todd, RIS-Corp, 5905 Weisbrook Lane, Suite 102 Knoxville, TN 37909, 2013.
- [22] R. deSouza, ZeptoSystems, Bloomington, IN, 2013.
- [23] G.L. Engel, et al., A multi-channel integrated circuit for use in low- and intermediate-energy nuclear physics—HINP16C, Nucl. Instrum. Methods A 573 (2007) 418–426, http://dx.doi.org/10.1016/j.nima.2006.12.052.

ARTICLE IN PRESS

L.A. McIntosh, A.B. McIntosh, K. Hagel et al.

Nuclear Inst. and Methods in Physics Research, A xxx (xxxx) xxx

[24]	M.	Youngs,	Using	light	emitted	clusters	as a	a probe	of the	symmetry	energy	ir
	the	nuclear	equation	on of	state (P	h.D. the	sis).	Michiga	n State	University	v. 2013.	

- [25] M.C. Solal, The origin of duo-lateral position-sensitive detector distortions, Nucl. Instrum. Methods A 572 (2007) 1047–1055, http://dx.doi.org/10.1016/j.nima. 2006.12.042.
- [26] C. Northcliffe, R. Schilling, Range and stopping-power tables for heavy ions, Nucl. Data Tables A7 7 (1970) 233–463, http://dx.doi.org/10.1016/S0092-640X(70) 80016-X.

[27]	F. Hubert, R. Bimbot, H. Gauvin, Range and stopping-power tables for 2.5-500
	MeV/nucleon heavy ions in solids, Atom. Data and Nucl. Data Tables 46 (1990)
	1-213. http://dx.doi.org/10.1016/0092-640X(90)90001-7.

[28]	M. Parlog, et al., Response of CsI(Tl) scintillators over a large range in energy
	and atomic number of ions. Part II: calibration and identification in the INDRA
6	array, Nucl. Instrum. Methods A 482 (2002) 693-706, http://dx.doi.org/10.
7	1016/S0168-9002(01)01712-0.
8	